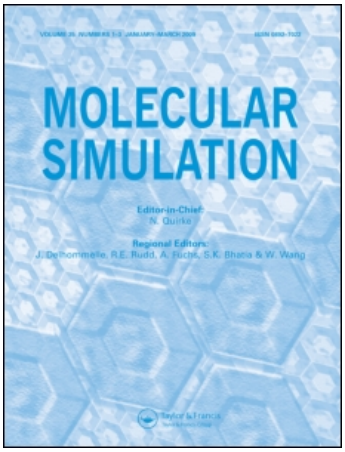

Molecular Simulation
Publication details, including instructions for authors and subscription information:
http://www.informaworld.com/smpp/title~content=t713644482

Nanocontraction flows of short-chain polyethylene via molecular dynamics simulations

Huan-Chang Tseng[a]; Jiann-Shing Wu[a]; Rong-Yeu Chang[b]
[a] Department of Applied Chemistry, National Chiao Tung University, Hsinchu, Taiwan, ROC [b] Department of Chemical Engineering, National Tsing Hua University, Hsinchu, Taiwan, ROC

To cite this Article Tseng, Huan-Chang , Wu, Jiann-Shing and Chang, Rong-Yeu(2009) 'Nanocontraction flows of short-chain polyethylene via molecular dynamics simulations', Molecular Simulation, 35: 8, 691 — 704
To link to this Article: DOI: 10.1080/08927020802651613
URL: http://dx.doi.org/10.1080/08927020802651613

Molecular Simulation
Vol. 35, No. 8, July 2009, 691–704

Taylor & Francis
Taylor & Francis Group

Nanocontraction flows of short-chain polyethylene via molecular dynamics simulations

Huan-Chang Tseng[a], Jiann-Shing Wu*[a1] and Rong-Yeu Chang[b]

[a]*Department of Applied Chemistry, National Chiao Tung University, Hsinchu, Taiwan, ROC;* [b]*Department of Chemical Engineering, National Tsing Hua University, Hsinchu, Taiwan, ROC*

(*Received 29 October 2008; final version received 27 November 2008*)

Nanocontraction flows of liquid short-chain polyethylene ($[CH_2]_{50}$) that were uniformly extruded by a constant-speed piston into a surrounding vacuum from a reservoir through an abrupt contraction nozzle were performed by employing molecular dynamics simulations. The extrudate exhibits a similar die swell phenomenon around the exit of the nozzle. In addition, numerous molecular chains are strongly adsorbed on the external surface of the nozzle. At high extrusion speeds, the velocity and temperature profiles in the nozzle show convex and concave parabolic curves, respectively, whereas the profiles are relatively flat at lower speeds. Near the internal boundary of the nozzle, the wall slip is inspected. Significantly, during the flow, the molecular chains undergo structural deformation, including compressed, stretched and shrunk motions. Comparisons with related experimental observations show that the simulated probability distributions of the bending and dihedral angles, and variations of the squared radius of gyration and orientations, are in reasonable agreement.

Keywords: nanocontraction flows; molecular dynamics simulations; Bio-MEMS; nanofluidics; polymer fluids

1. Introduction

Understanding the microscopic-level information with respect to transportation, deformation and orientation of molecular chains flowing during varying macroscopic channels is of considerable importance, especially for bio-micro-electro-mechanical systems (Bio-MEMS) techniques [1–3]. Contraction flows have been the focus of a vast amount of research devoted to computational fluid dynamics (CFD) of polymer fluids [4,5], such as generally appearing in the extrusion processes. Die/extrudate swell in the contraction flow is a significant phenomenon describing the increase in the diameter of a liquid jet, or extrudate, as it exits the nozzle or die [4,6,7].

In recent years, the motions of deoxyribonucleic acid (DNA) molecules, limited in microcontraction channels, have become vital knowledge in Bio-MEMS, in seeking examples of biochip devices [1–3,8]. Previous experimental studies typically used an atomic force microscope (AFM) [9] to directly observe the motion of DNA molecules in microfluidic devices [1–3]. Such studies indicated that as DNA molecules entered the narrow nozzle, they were stretched dramatically through pure shear flow, whereas DNA molecules flowing in the internal region of the nozzle were stretched considerably by pure elongation flow. Most of the studies, thus far, have primarily adopted CFD computations to simulate such microscopic flow phenomena [10].

Occurring in a practical micro/nanochannel, however, flow behaviours may be influenced by the scaling, surface wetting and boundary slip effects in the non-continuum fluid field [11]. When traditional approaches of Navier–Stokes theoretical predictions are directly applied, their ability to probe the molecular-level phenomena becomes inadequate and unpredictable. To treat these issues, methods for researching molecular fluids need to be redefined and reconsidered on the basis of molecular motions. Molecular dynamics (MD) simulation methodology describes a variety of molecular motions according to Newton's equation of motion. Up to now, MD simulation has been widely applied to material science, molecular biology and nanofluidic mechanics.

Over the past two decades, a number of studies with respect to the boundary slip phenomenon for simple fluid argon (Ar) gas by MD simulation have been conducted on simple flow fields, namely both simple shear and Poiseuille flows [12,13]. Using non-equilibrium MD (NEMD) simulations, Moore et al. [14] and Jabbarzadeh et al. [15] predicted nanorheological properties of polymer fluids in bulk and thin films, respectively, including the shear-rate dependence of the viscosity, as well as the first and second normal stress differences/coefficients under shear.

Recently, Wang and Sandberg [16] mimicked free and tethered DNA molecules in a nanochannel by employing chemistry at Harvard macromolecular mechanics software. Their results clearly indicated that the molecules underwent stretching, rotating and relaxing motions in the nanochannel. It is noteworthy that Tseng et al. [17] presented NEMD discussions on liquid *n*-hexadecane in terms of the variations of shear thinning and shear

*Corresponding author. Email: inblue.ac89g@nctu.edu.tw

ISSN 0892-7022 print/ISSN 1029-0435 online

DOI: 10.1080/08927020802651613
http://www.informaworld.com

dilatancy, along with different temperatures, pressures and densities. Additionally, using the Arrhenius equation and Barus equation, they assessed the flow activation energy and the pressure–viscosity coefficient, respectively, which were in good agreement with related MD and experimental studies.

The applications of MD studies on the complex geometric flows have been conducted with respect to nanocontraction expansion flow and nanojet. The findings of nanocontraction expansion flow of Ar fluid by Fan et al. [18] showed a vortex at the corner, which was in agreement with macroscopic experimental observations. In particular, Moseler and Landman [19] performed the nanojet system, the diameter of the gold nozzle being 6 nm and the fluid contained 200,000 propane molecules. Their significant observations indicated the formation, stability and break-up of nanojet at various pressures. Shin et al. [20] discussed the influence of varying the diameters of the nozzle on thermodynamic properties of nanojet for Ar fluid. Murad and Puri [21] designed a nanojet colliding system utilising water molecules and found a recoil phenomenon following head-on collisions. They suggested that the duration between collision and recoil was a function of the nanojet impact velocity and intermolecular interactions. Dai and Chang [22] revealed a linear relationship between the length of liquid threads and the compressing velocity in nanojet processes for liquid propane.

Reviewing the aforementioned studies of the nanojet, however, most of the focus is limited with respect to simple molecules involving Ar, water and propane. As for long molecular chains, MD investigations have seemingly been ignored in the discussions on complex geometric flows. Our simple motivation is that an increase in the molecular length will make an enhancement in the degree of non-Newtonian flow behaviours. In this regard, based on our previous studies [17,22], *n*-hexadecane shear flow and propane nanojets, the objective of the present study is further extended in observing nanocontraction flow phenomena of short-chain polyethylene (PE) fluid. Our PE fluids are $[CH_2]_{50}$ chains, which belong to long chains in contrast to *n*-propane (C_3H_8) and *n*-hexadecane ($C_{16}H_{34}$) molecules. In addition, our geometry of the system with a planar abrupt contraction nozzle with a 4:1 aspect ratio consists of gold atoms comprising face-centred cubic (FCC) lattice cells.

In Section 2, we briefly describe simulation details. Three primary focuses are presented in Section 3. First, we observe nanocontraction flow phenomena and motions of molecular chains during the flow. Second, we can qualitatively determine motions of molecular chains, such as compressed, stretched and shrunk motions in the contraction flow field, through the tendencies to variations of molecular structural properties, which include the probability distribution of bond bending and torsions, as well as squared radius of gyration and the degrees of orientation. Third, we would like to understand the nozzle flow field, especially for the velocity and temperature profiles. Furthermore, all properties are discussed at different extrusion speeds. In Section 4, we summarise conclusions and make suggestions for future studies.

2. Simulation details

The molecular chain is modelled with the use of spherical interaction sites, regarded as methylene (CH_2) groups. Interaction sites connected together can form molecular chains. This coarse-grained model, which is known as the united atom (UA) model, is widely used in related studies such as those on alkane molecules [23] and PE chains [24]. The descriptions of molecular chains are dominated by van der Waals (vdW) interaction and covalent bonding interactions, which involve bond stretching, bond bending and torsion motions of molecules.

In the present study, the modelling of the motions of molecules mentioned above is based on the set of realistic potential models of Chynoweth et al. [25] and Chynoweth and Michopoulos [26] (CM), who fit optimal parameters of the vdW potential using experimental data on the heat enthalpy of vaporisation. Overall, the CM model predicted rheological properties of shear flows better than 'the transferable potential for phase equilibria (TraPPE)' model [27], which is an adaptation for calculating the vapour–liquid coexistence curve and the surface tension of *n*-alkane phase diagrams. By contrast, in predicting thermodynamic properties, the TraPPE model is superior to the CM model [17]. Thereby, 50 CH_2 groups of short-chain PE in the present study can be directly extended, largely increasing from the 16 CH_2 groups of the *n*-hexadecane in our previous study [17] regarding the thermodynamic and rheological discussions of steady shear flows.

For completeness, we briefly describe the CM model governing the flexibility of molecular chains, which contains the vdW interaction and covalent bonding interaction, as follows:

i) *vdW interaction*. The vdW potential U_{LJ} can be represented by the 12–6 Lennard-Jones (LJ) potential,

$$U_{LJ} = 4\varepsilon_{LJ}\left[\left(\frac{\sigma_{LJ}}{r_{ij}}\right)^{12} - \left(\frac{\sigma_{LJ}}{r_{ij}}\right)^{6}\right], \qquad (1)$$

where r_{ij} is the distance between two CH_2 groups, and ε_{LJ} and σ_{LJ} are the energy and length parameters of the LJ potential, respectively, for the pair of groups *i* and *j*. To reduce the computational time of the vdW force, the shifted LJ potential [28] is usually

truncated at a cut-off distance r_c (in this case, $r_c = 2.5\ \sigma_{LJ}$ or 1.01 nm), so that $U_{LJ}(r_c) = 0$.

ii) *Covalent bonding interaction*. The bond-stretching potential U_s connects two CH_2 groups by Hooke's harmonic potential,

$$U_s = \frac{1}{2}k_l(l_i - l_0)^2, \tag{2}$$

where k_l is the bond-stretching energy constant and l_i is the bond length between groups $i-1$ and i.

The bond-bending potential U_b is described by the Taylor series' cubic term expansion of the bending angle deviation

$$U_b = \frac{1}{2}k_\theta\left[(\theta_i - \theta_0)^2 - k'_\theta(\theta_i - \theta_0)^3\right], \tag{3}$$

where k_θ is the bond-bending energy constant, k'_θ is the bond-bending angle constant, and θ_i is a bond angle among three adjacent CH_2 groups $i-1$, i and $i+1$.

The torsion potential U_t is expressed by a fifth-order cosine polynomial of a dihedral angle,

$$\begin{aligned} U_t =& c_0 + c_1\cos\phi_i + c_2\cos^2\phi_i + c_3\cos^3\\ &\phi_i + c_4\cos^4\phi_i + c_5\cos^5\phi_i, \end{aligned} \tag{4}$$

where $\{c_n\}$ are the values of the set of torsion energy coefficients, and ϕ_i is the dihedral angle formed by four consecutive CH_2 groups $i-1$, i, $i+1$ and $i+2$. All parameters for the potential models are listed in Table 1.

As for the interaction between PE fluid and gold wall that consisted of CH_2 groups and Au atoms, respectively, it is necessary to specify the interaction between the CH_2 groups and Au atoms by the 12–3 LJ model of the typical semi-empirical potential function [29], which is as follows:

$$U_{CH_2-Au} = 2.117\varepsilon_{CH_2-Au}\left[\left(\frac{\sigma_{CH_2-Au}}{r_{ij}}\right)^{12} - \left(\frac{\sigma_{CH_2-Au}}{r_{ij}}\right)^{3}\right], \tag{5}$$

where σ_{CH_2-Au} (0.3495 nm) and ε_{CH_2-Au} (0.432 kJ mol^{-1}) are the energy and length parameters between the CH_2 groups and Au atoms, respectively. The cut-off distance of the 12–3 LJ potential of the CH_2–Au interaction is 1.62 nm (4.0 σ).

In addition, the piston, reservoir and nozzle are formed by the Au atom layer of FCC lattices with a lattice constant of 0.4050 nm. The interaction between the Au atoms is modelled by the Morse potential [30], which is as follows:

$$U_{Morse} = D\left[e^{-2\alpha(r_{ij}-r_0)} - 2e^{-\alpha(r_{ij}-r_0)}\right], \tag{6}$$

where D (45.839 kJ mol^{-1}) is the cohesion energy and r_0 (0.3024 nm) is the equilibrium distance between the Au atoms; α controls the 'width' of the potential and equals 15.830 nm^{-1}. The cut-off distance of the Morse potential is 1.42 nm (3.5 σ).

Equations of motion [28] for a simulation system consisting of the total number (N) of both fluid and wall atoms are

$$\mathbf{p}_i = m_i\dot{\mathbf{r}}_i, \tag{7}$$

$$\dot{\mathbf{p}}_i = \mathbf{F}_i, \tag{8}$$

where m_i is the mass of the ith atom, $\mathbf{r}_i$ is the position vector of the ith atom, $\mathbf{p}_i$ is the peculiar momentum of the ith atom, and $\mathbf{F}_i$ is the interaction force on the ith atom. For a flow system, the peculiar momentum [15] of the ith atom is defined by

$$\mathbf{p}_i = m_i(\mathbf{v}_i - \mathbf{U}_i), \tag{9}$$

where $\mathbf{v}_i$ is the instantaneous velocity of the ith atom and $\mathbf{U}_i$ is the stream velocity of the ith atom; then, the temperature on the atomic level requires the calculation of the peculiar momentum. Thus, the temperature T of MD simulations [28] was easily evaluated in terms of the microscopic variable, which is as follows:

$$\langle T\rangle = \left\langle \frac{1}{3Nk_B}\sum_{i=1}^{N}\frac{\mathbf{p}_i^2}{m_i}\right\rangle. \tag{10}$$

With respect to the solid state of the Au atoms of the wall part, the *ad hoc* velocity-rescaling method [28] is commonly employed to constrain the temperature of all

Table 1. The potential parameters of LJ and covalent bonding interactions.

Parameter	Value	Unit
LJ		
σ_{LJ}	4.045	Å
ε_{LJ}	0.420	kJ mol^{-1}
Bond stretching		
k_l	2650.98	kJ mol^{-1} Å^{-2}
l_0	1.53	Å
Bond bending		
k_θ	0.1004	kJ mol^{-1} deg^{-2}
k'_θ	0.0096	deg^{-1}
θ_0	109.47	deg
Torsion		
c_0	9.278	kJ mol^{-1}
c_1	12.155	kJ mol^{-1}
c_2	−13.119	kJ mol^{-1}
c_3	−3.060	kJ mol^{-1}
c_4	26.239	kJ mol^{-1}
c_5	−31.493	kJ mol^{-1}

the wall atoms in the present study, which is as follows:

$$\mathbf{p}_{i,\mathrm{new}} = \beta \mathbf{p}_i, \tag{11}$$

$$\beta^2 = 3N_{\mathrm{w}} k_{\mathrm{B}} T_{\mathrm{d}} / \sum_{i=1}^{N_{\mathrm{w}}} \frac{\mathbf{p}_i^2}{m_i}, \tag{12}$$

where β is a rescaling factor, $\mathbf{p}_{i,\mathrm{new}}$ is the new momentum of the ith atom after correction, N_{w} equals the total number of wall atoms, k_{B} is Boltzmann's constant (1.381×10^{-23} J/K), and T_{d} is the desired temperature of 400 K in the present study. This method offers the advantage of a simple algorithm, albeit the lack of a convincing derivation of physical theory is its disadvantage. Under the condition of the atom's position shifting minutely, the *ad hoc* velocity-rescaling method is advisably applied in the solid state.

Furthermore, as the variation in the liquid fluid's atomic positions is larger than in a solid, the Nosé–Hoover thermostatting algorithm [28,31], which possesses the canonical ensemble in statistical mechanics, is adopted to obtain a more precise position and momentum of the atom,

$$\dot{\mathbf{p}}_i = \frac{1}{m_i}\mathbf{F}_i - \eta \mathbf{p}_i, \tag{13}$$

$$\dot{\eta}(t) = \frac{1}{Q}\left[\sum_{i=1}^{N_{\mathrm{f}}} \frac{\mathbf{p}_i^2}{m_i} - g k_{\mathrm{B}} T_{\mathrm{d}}\right], \tag{14}$$

$$Q = g k_{\mathrm{B}} T_{\mathrm{d}} \tau^2, \tag{15}$$

where η is the friction coefficient, Q is the mass of the thermal bath, g is the number of degrees of freedom, τ is a characteristic thermostat relaxation time of 0.1 ps, and N_{f} equals the total number of the CH_2 groups of the PE fluid. The Nosé–Hoover algorithm belongs to the integral feedback regulation method, as shown in Equation (13). The basic concept of this method, which solves a first-order ordinary differential equation of momentum, is very different from the *ad hoc* velocity-rescaling method of Equation (11). Note that the equations of motion mentioned above are performed by Gear's fifth-order predictor–corrector algorithm [28]. The magnitude of time step depends on an extrusion speed from 0.8 to 0.1 fs, due to ensuring numerical stability.

Moreover, one of the measures of a chain's dimension is the squared radius of gyration [24], defined via

$$\left\langle R_{\mathrm{g}\alpha}^2 \right\rangle = \frac{1}{n}\sum_{i=1}^{n} \left\langle (r_{i\alpha} - r_{\mathrm{cm}})^2 \right\rangle, \tag{16}$$

where n is the number of UAs per chain molecule ($n = 50$ in the present study), $r_{i\alpha}$ is the αth ($\alpha = x$, y or z) component of the position of the ith atom, and r_{cm} is the position vector of the centre of mass of the individual chain. In general, the degree of molecular orientation S [24] can also be directly determined by the end-to-end vector $\mathbf{e}$ of the individual molecular chain,

$$\langle S_\alpha \rangle = \frac{3\left\langle \cos^2 \psi_\alpha \right\rangle - 1}{2}, \tag{17}$$

where S_α is the degree of the molecular orientation along the α-axis, and ψ_α is the angle between $\mathbf{e}$ and the α-axis. When $\mathbf{e}$ is parallel, random or perpendicular to the α-axis, parameter S_α equals a value of 1.0, 0.0 and -0.5, respectively.

Finally, for obtaining time averages of statistical properties, we must collect original data every two time steps during run processes. By the simple moving average method [32], which is frequently used to analyse time-series data, each time-averaged value is performed by 20,000 samples over the rest of our simulation. To explore molecular motions, this statistic method was adopted to analyse some molecular structural properties, which contain the bond length and the bond angle, as well as the squared radius of gyration and the degree of orientation.

3. Results and discussion

Following our previous study [17] on simple steady shear flow for liquid *n*-hexadecane molecular fluid, the present study further extends the advance regarding the fluid's molecular length and system geometry, to establish an MD computational framework of nanocontraction flow. Such a flow system contains three parts: a piston, a reservoir and a nozzle. The schematic of the system is illustrated in Figure 1(a). The periodic boundary condition [28] is applied in the y-direction of the flow system.

PE fluid is extruded by a planar piston into a surrounding vacuum from a reservoir through a planar abrupt contraction nozzle with a 4:1 aspect ratio. The width of the nozzle (D_{n}) is 2.7 nm. The body of the extruded fluid outside the exit of the nozzle is usually called 'the extrudate' [7]. The materials of the piston, reservoir and nozzle consist of 34,000 gold wall (Aurum, Au) atoms comprising FCC lattice cells. The PE fluid is composed of 576 linear molecular chains $[CH_2]_{50}$ of a random configuration. The PE fluid and the Au wall density are 0.75 and 19.70 g/cm^3, respectively. During the simulation process, a piston constrainedly moves to a constant distance of 10.11 nm along the x-direction at a constant speed, and then stops, while the stationary liquid of $[CH_2]_{50}$ in the reservoir is pushed into the nanonozzle. Thus, this procedure is one of generating contraction flow behaviour; additionally, the extrusion speed corresponds to the piston moving speed.

Notably, in the very long initial equilibrium stage, all wall and fluid atoms maintain a constant temperature of 400 K, together. Once the flow process starts, in order

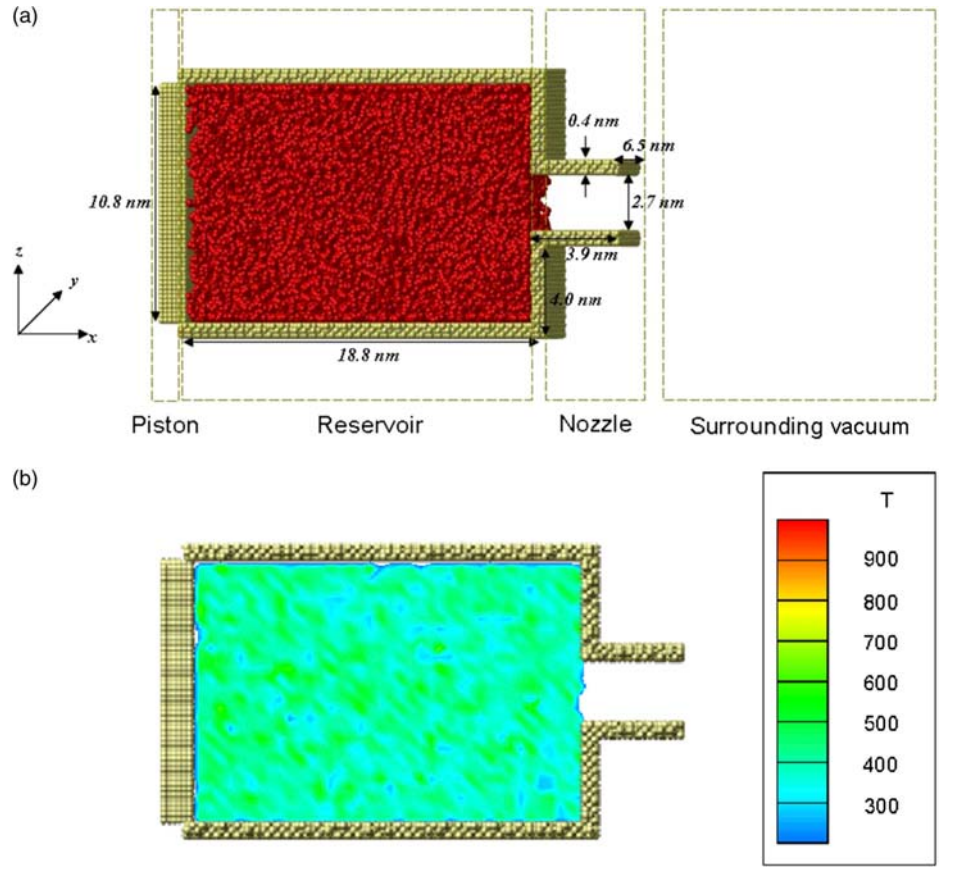

Figure 1. (a) A schematic of the planar nanocontraction flow system. The red and gold components are CH_2 groups and Au atoms, respectively; (b) a temperature contour of the reservoir displays a uniform colour distribution of the average temperature of 400 K at the initial equilibrium stage.

to make an isothermal boundary, only the wall part needs to maintain an isothermal state at 400 K. The fluid part is compulsorily made a non-isothermal state; namely, the Nosé–Hoover thermostatting algorithm [28,31] in the program is shut off for all atoms of the extruded fluid.

Since the equilibrium melting temperature of PE is about 414 K [24], the fluid should be of a liquid state so that the PE fluid at 400 K should be successfully transported in the contraction flow system. Overall, we expect that such a flow system is in an unsteady state and non-thermal one. As shown in Figure 1(b), in the initial isothermal equilibrium stage, the temperature contour in the reservoir almost displays a uniform distribution at an average temperature of 400 K. This temperature contour represented an isothermal system.

We have organised the results of nanocontraction flow phenomena for the PE fluid with respect to varying extrusion speeds into three sections, which are as follows:

(1) In Section 3.1, we observe significant flow characteristics by coloured snapshots and temperature contour pictures.
(2) In Section 3.2, we predict molecular structural properties, including the probability distribution of bond bending and torsion, and their overall changes in the squared radius of gyration as well as the degrees of orientation.
(3) In Section 3.3, we present both the temperature and velocity profiles at the nanonozzle when the fluid steadily flows through the nozzle channel.

3.1 Characterisations of a nanocontraction flow

3.1.1 A constant extrusion speed of 86.4 m/s

Here, one of the objectives of the present study is the observations of nanocontraction flow behaviours. In Section 3.1.2, the effect of the extrusion speed on flow behaviours is discussed. During the initial equilibrium stage of the simulation, the temperature and pressure of the fluid in the reservoir converged at 400.04 ± 0.06 K and 33.4 ± 0.35 MPa, respectively, indicating that the state point of the fluid reached a thermodynamic equilibrium. As the system reached such a state point, we began progressing simulations of the contraction flow process.

The piston moved to a distance of 10.11 nm along the x-direction at a constant extrusion speed of 86.4 m/s. As shown in Figure 1, the fluid was pushed through the nozzle from the reservoir by a piston into a vacuum. Initially, no molecular chains exited the nozzle at the onset of the piston movement; after the piston moved at a time interval of about 34.4 ps, the first whole molecular chain was observed leaving the nozzle exit. When the fluid exited the nozzle, many molecular chains of the extrudate were adsorbed on the external surface of a nozzle. This phenomenon is known as surface wetting.

Significantly, Figure 2(g) shows that the maximum diameter of the extrudate, D_f, was about 8.45 nm, which is considerably larger than the nozzle width, D_n, of 2.7 nm. The swell ratio (D_f/D_n) was nearly 3:1. This is analogous to the die swell in the traditional polymer extrusion process. Such wetting and swell phenomena are in agreement with the nanojet study of Moseler and Landman [19]. In Figure 2(h), the extrudate had broken up in the vicinity of the nozzle exit while its molecular chains had a slight disentanglement behaviour.

In general, a molecular chain $[CH_2]_{50}$, which has fully developed to a *trans* conformation, has a zigzag shape and a length of about 6.08 nm. Since the length of a molecular chain is larger than the nozzle diameter of 2.7 nm, we were interested in understanding how a molecular chain flows through the nozzle region. To explore molecular motion during the contraction flow, we visualised only 20 molecular chains distributed over the reservoir, which are shown in different colours in Figure 3. Some molecular chains were observed to be gradually compressed during the ceaseless movement of the piston.

When each molecular chain neared the interface between the reservoir and the nozzle, it was strongly stretched and instantaneously entered the nozzle. As a molecular chain flowed through the geometric constraint of the nozzle, it was stretched and orientated along the flow direction. When the stretched molecular chain exited the nozzle, it promptly shrank back to a stable state,

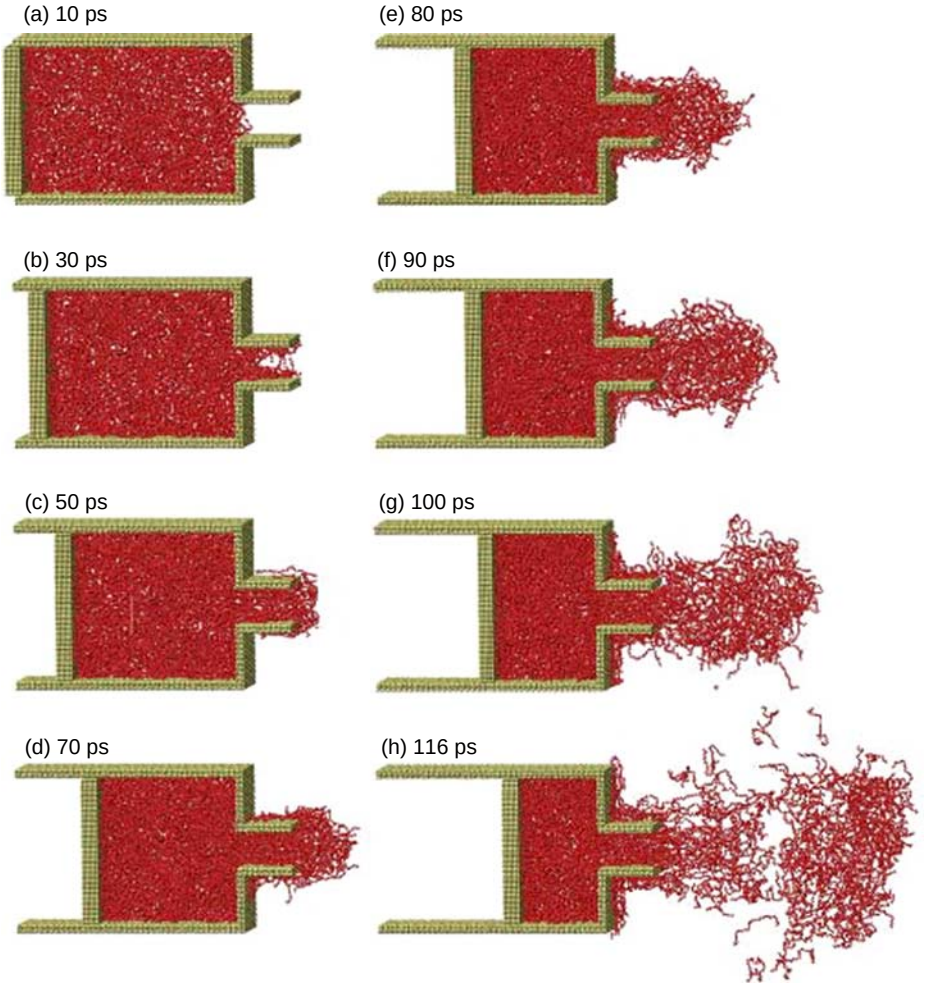

Figure 2. The extrusion speed is set at 86.4 m/s. Snapshots (a)–(h) of the whole PE fluid show the history of the nanocontraction flow as a piston moves a distance of 10.11 nm: (a) 10 ps, (b) 30 ps, (c) 50 ps, (d) 70 ps, (e) 80 ps, (f) 90 ps, (g) 100 ps, and (h) 116 ps.

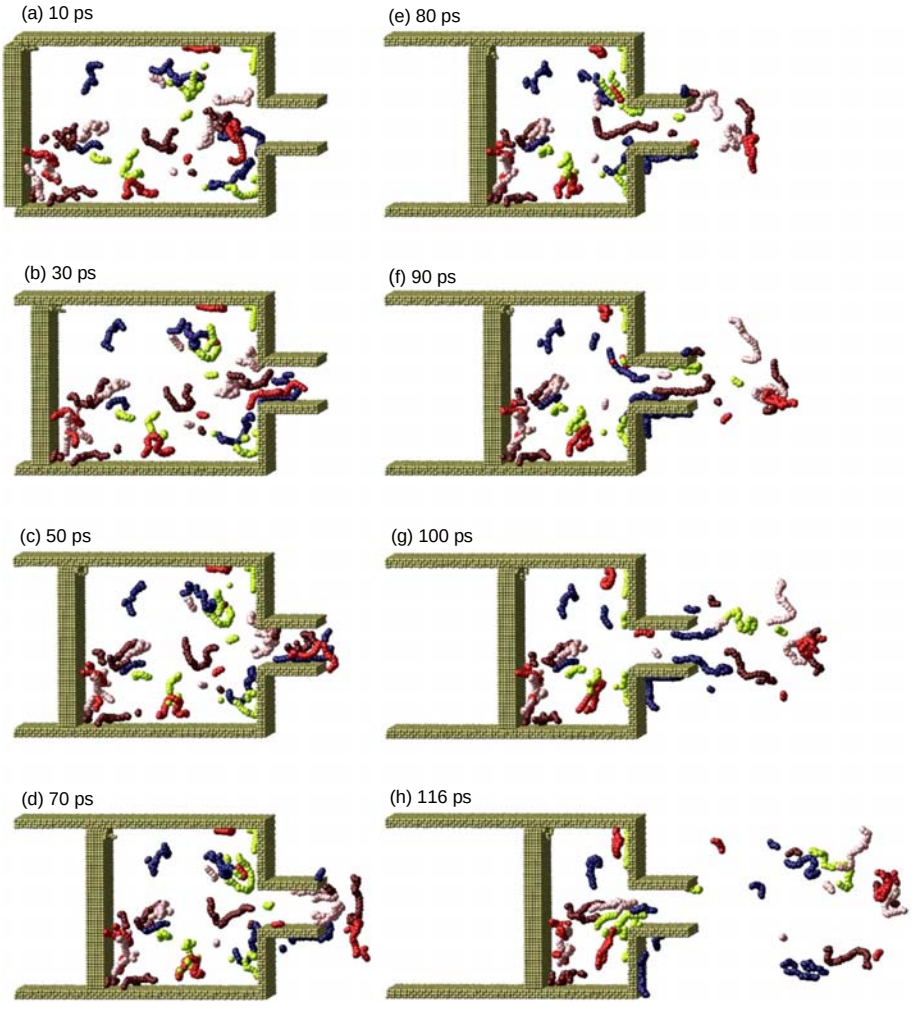

Figure 3. The extrusion speed is set at 86.4 m/s. These snapshots show the deformation of molecular motion for 20 molecular chains, shown in five colours, at the reservoir, abrupt contraction nozzle and the vicinity around the nozzle exit. Observations are shown at the following time intervals: (a) 10 ps, (b) 30 ps, (c) 50 ps, (d) 70 ps, (e) 80 ps, (f) 90 ps, (g) 100 ps, and (h) 116 ps.

namely random coil configuration. Our MD observations are similar to the AFM experimental observations of Shrewsbury et al. [1], who found that a DNA molecule was also stretched in a microfluidic device's contraction flow field. In Section 3.2.2, we quantitatively discuss these molecular motions during the flow through variations in both the squared radius of gyration and the degree of orientation.

3.1.2 Varying extrusion speeds between 10.8 and 86.4 m/s

As shown in Section 3.1.1, nanocontraction flow has two phenomena: the surface wetting of the nozzle and the similar die swell of the extrudate. Here, we would like to understand how both phenomena are influenced by extrusion speeds, which are as follows. The four extrusion speeds are 10.8, 21.6, 43.2 and 86.4 m/s. In Figure 4, snapshots of the contraction flow are presented in which a piston has moved a distance of 10.11 nm. At the lower extrusion speed of 10.8 m/s, many molecular chains were adsorbed on the outer surface of the reservoir. This result suggested that the attractive forces between the Au atoms and CH_2 groups may be strong due to the 12–3 LJ potential (cf. Equation (5)) used in the simulation, while the number of adsorbed molecular chains decreased with increasing extrusion speed.

As for the actual die swell phenomenon, polymer fluids possess a very high degree of entanglement for molecular chains. In particular, Foteinopoulou et al. [33] demonstrated that once the chain length of PE is larger than about 200 UAs, it starts generating entanglement. Thus, our short-chain PE, $[CH_2]_{50}$, should not exhibit such an obvious entanglement feature. In this regard, we do not purpose to investigate the die swell in depth for $[CH_2]_{50}$.

As molecular chains of the extrudate may cohere and attract each other, the overall body of the extrudate

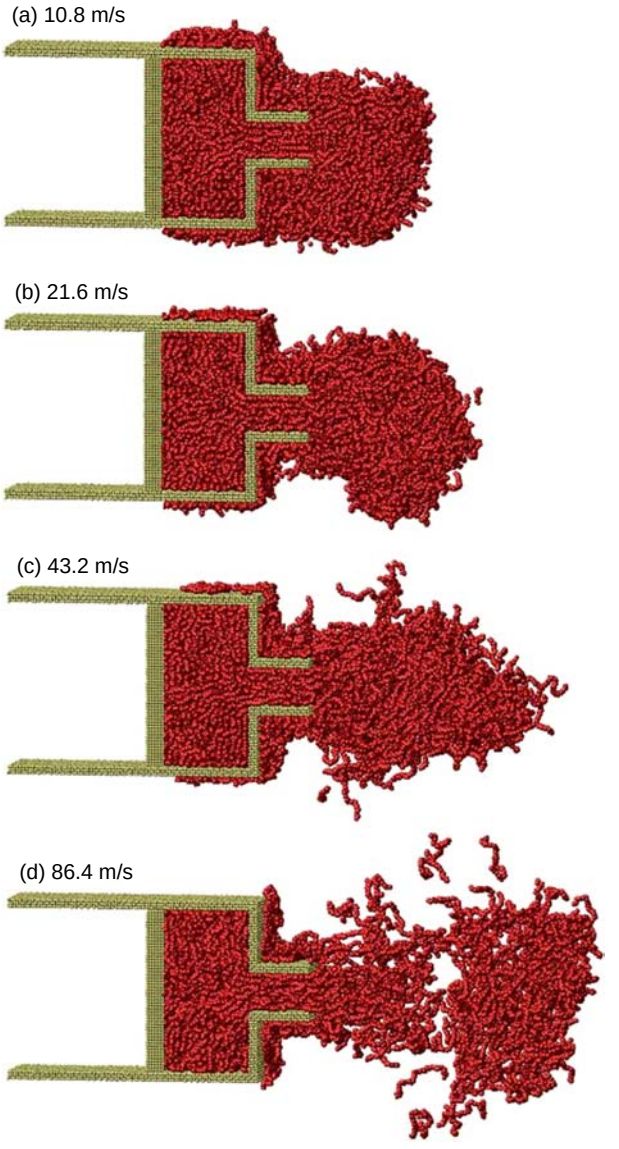

Figure 4. Snapshots of the contraction flow shown at different extrusion speeds when a piston has travelled a distance of 10.11 nm: (a) 10.8 m/s at 928 ps, (b) 21.6 m/s at 464 ps, (c) 43.2 m/s at 232 ps, and (d) 86.4 m/s at 116 ps.

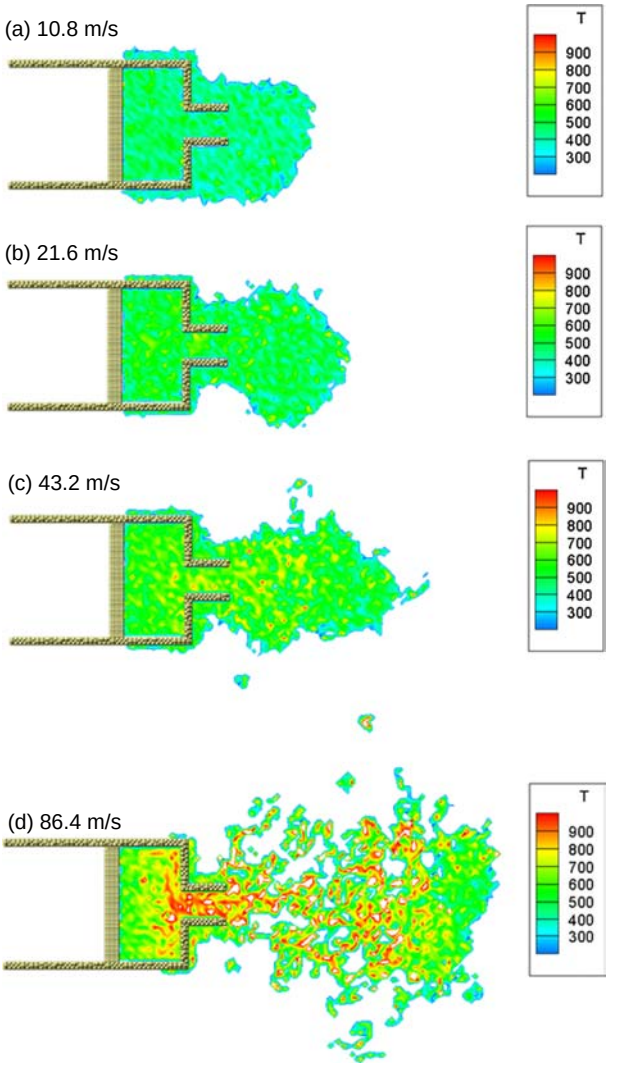

Figure 5. Temperature contours of the contraction flow at different extrusion speeds when the piston has travelled a distance of 10.11 nm: (a) 10.8 m/s at 928 ps, (b) 21.8 m/s at 464 ps, (c) 43.2 m/s at 232 ps, and (d) 86.4 m/s at 116 ps.

virtually maintains a continuous structure in the speed region of 10.8–43.2 m/s. The ratio of the swell for the extrudate decreased with increasing speed. In the past, the macroscopic experimental results of Graessley et al. [6] focused on the relationship between a decrease in the swell ratio and an increase in the Reynolds number; also, the macroscopic simulation results of Han et al. [4] presented the relationship between a decrease in the swell ratio and an increase in the shear rate by the finite-difference method (FDM). Although the fluid specimen and flow operation are somewhat different, our results are in qualitative agreement with macroscopic results. In Figure 4(d), as the extrusion speed reached the maximum of 86.4 m/s, the front of the extrudate was similar to the free jet flow. The molecular chains of the extrudate exhibited a slightly scattered state. Incidentally, we found that the projected distance of the extrudate increased with the extrusion speed.

As mentioned above, we expect that the PE fluid is in an unsteady and non-isothermal state during the flow process. Such a state is observed through the temperature contour plot of the fluid. As shown in Figure 5, the temperature contours evolved gradually from a single colour pattern to a vivid pattern as the extrusion speed doubled from 10.8 to 86.4 m/s, where the piston had travelled a distance of 10.11 nm. The overall temperature of the fluid increased with the extrusion speed.

As a result, there are two features for the fluid temperature distribution. First, at 10.8 and 21.6 m/s, the

temperature contours remained almost uniform between about 400 and 500 K; as one would expect, the overall temperature of the fluid was higher at 21.6 m/s than that at 10.8 m/s. Second, at 43.2 and 86.4 m/s, the temperature of the fluid front was lower than that of the internal extrudate; thus, our observations of the temperature contour are also similar to the results of Shin et al. [20] who researched thermodynamics properties of nanojet for Ar particles.

Eventually, at the highest extrusion speed of 86.4 m/s, the temperature of the extrudate was maintained between 800 and 1000 K, and the temperature of the fluid in the nozzle region was higher than that of the extrudate. Such a high temperature should cause the extrudate to break up and the molecular chains of the extrudate to separate. Accordingly, we conjecture, with caution, that the contractive geometry of the present study may be associated with a higher potential energy so that the fluid possesses a higher temperature at an extreme extrusion speed.

3.2 Molecular-level information of a nanocontraction flow

3.2.1 Intrinsic structure characteristics of molecule chains

To understand the variations in molecular intrinsic structures at the reservoir, we measure the bond length and the bond angle of molecular chains. Based on our previous study [17], the potential model constrains that the equilibrium bond length and the bond angle are approximately 0.153 nm and 109.47°, respectively. As shown in Figure 6(a) and (b), the average bond length and the bond angle in the initial period are 0.150 nm and 108.72°, respectively. This means that the molecular chains are compressed at the reservoir.

When the piston moved continually, the bond length of the molecules was obviously shortened. Simultaneously, the bond angle maintained mostly small fluctuation between 108.72° and 108.74°; it is close to the initial bond angle of 108.72°. In other words, the movement of the piston does not strongly affect the bond angle. Thus, we suggest, with caution, that the bond length and the bond angle may possess elastic and rigid characteristics, respectively.

As to the probability distributions of the bond length and bond angle for all molecular chains of the fluid, Figure 7(a) and (b) shows that the peaks of the curves occur at an equilibrium bond length of 0.153 nm and an equilibrium bond angle of 109.47°, respectively. The peaks correspond to the highest probability of the respective structure characteristics. Both height probabilities decreased as the extrusion speed increased. As a whole, the bond length distribution ranged between 0.132 and 0.172 nm, and the bond angle distribution between 89.7° and 131.1°.

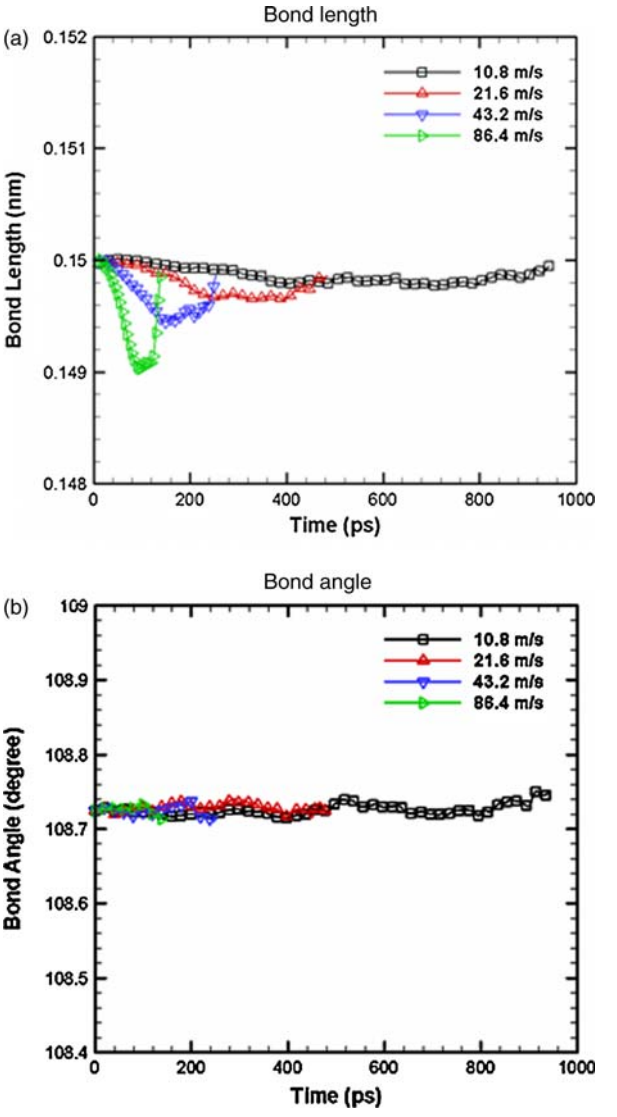

Figure 6. (a) Bond length and (b) bond angle of molecular chains at the reservoir *versus* time t at the different extrusion speeds.

Such probability distributions allow us to understand the effect of stretch and compression for molecular chains on the potential energy.

Furthermore, the probability distribution of the dihedral angle ϕ_i in Figure 7(c) indicates the highest probability at two locations of 0° and 360°. Both angles correspond to the *trans* conformation, which possesses the lowest energy state of the dihedral angle potential [34]. As the extrusion speed increased, the probability of the *trans* conformation fell. Moreover, the *gauche* conformations, both g^+ and g^- at $\phi_i = \pm 120°$, indicate the second highest probability distribution. The number of *gauche* conformations had no relevance to the extrusion speed. A very higher energy state at $\phi_i = 180°$ is of the *cis* conformation. In the present study, such an unstable

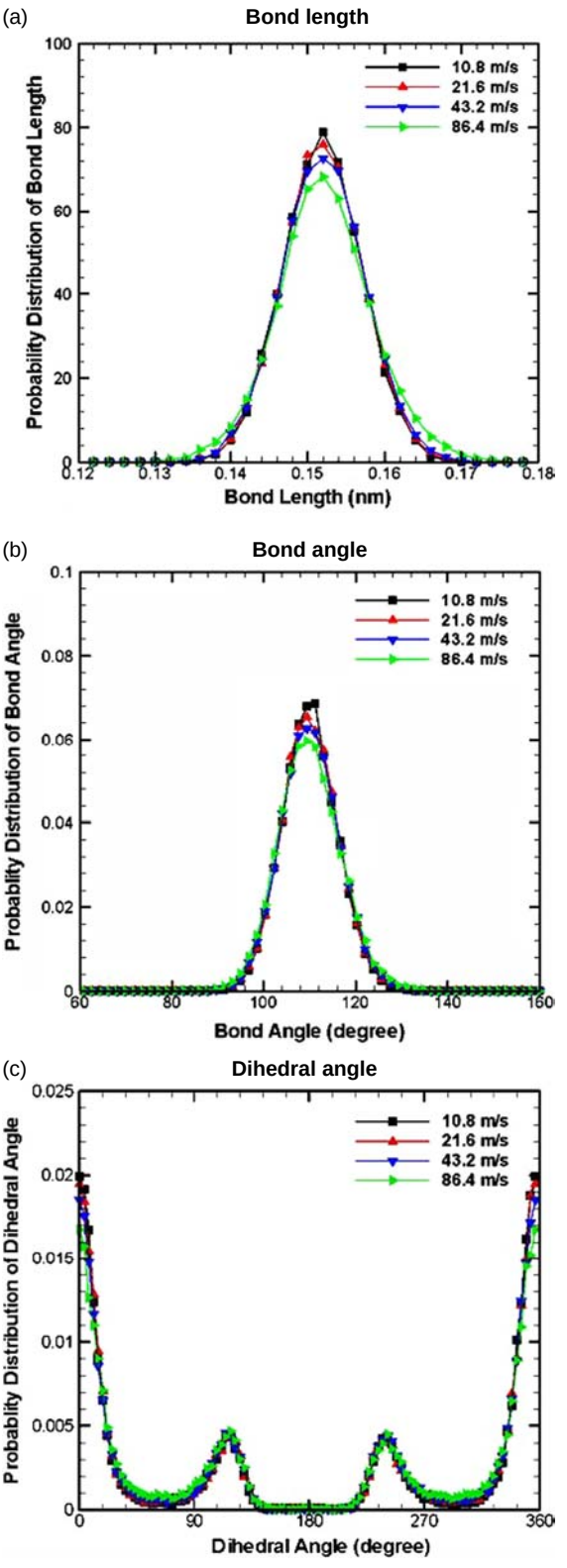

Figure 7. (a) Bond length, (b) bond angle and (c) dihedral angle distributions of all molecular chains *versus* different extrusion speeds when the piston had travelled a distance of 10.11 nm. Note that the equilibrium bond length and angle are 0.153 nm and 109.47° in this study, respectively.

conformation's probability was nearly zero. These observations are similar to the MD findings of Jabbarzadeh et al. [15], who showed the effects of the shear rate on the probability distribution of the molecular structure for liquid *n*-hexadecane in steady shear flows.

3.2.2 *Conformation and orientation of molecular chains*

Another goal of the present study is to reveal the motions of molecular chain during the nanocontraction flow process through tendencies to variations of the chain's conformation and orientation. The dimensions of molecular chains can be estimated by the squared radius of gyration [24], R_g^2, according to Equation (16). This is helpful in understanding the deformation procedure of molecular chains in the three areas of the simulation system: the reservoir, nozzle and surrounding.

In the initial equilibrium state, the variation in R_g^2 at the reservoir consisted of three components: R_{gx}^2, R_{gy}^2 and R_{gz}^2 converging to 0.43, 1.11 and 0.32 nm^2, respectively. Since the periodic boundary condition was dictated in the *y*-direction of the reservoir, the motion of molecular chains was easily extended in the *y*-direction. Thus, R_{gy}^2 was the greatest value in the three directions. R_{gz}^2 was shorter than R_{gx}^2 due to the smallest size of the reservoir in the *z*-direction.

At the reservoir, Figure 8(a) shows the variations in R_{gx}^2 along successive time intervals for different extrusion speeds. R_{gx}^2 decreased with increasing operation time of the piston movement; namely the molecular chains at the reservoir are compressed. Specifically, at lower extrusion speed of 10.8 m/s, the R_{gx}^2 variation is relatively unobvious. As depicted in Figure 8(b), at the nozzle region, R_{gx}^2 were greatly lengthened with the operation time; this indicates that the molecular chains are stretched at the nozzle. By analysing Figure 8(a) and (b), the difference between the R_{gx}^2 variations of the reservoir and the nozzle is evident. The R_{gx}^2 value at the nozzle is approximately five times greater than that at the reservoir. This comparison points out that the molecular motion of the flow field is strongly affected by the geometric change occurring between the reservoir and the nozzle. Incidentally, in the present study, we also observed that the *z*-directional component of the squared radius of gyration R_{gz}^2 correspondingly increased in the reservoir and decreased in the nozzle; thus, the molecular chain's size became extended in the reservoir and shrank in the nozzle.

When the molecular chains left the nozzle to approach a very wide surrounding vacuum, the R_{gx}^2 variation of the extrudate is shown in Figure 8(c). The change in R_{gx}^2 between the nozzle and the surrounding vacuum can be inspected via the analysis of Figure 8(b) and (c). Figure 8(b) and (c) indicates that the R_{gx}^2 values in the surrounding vacuum are smaller than those at the nozzle; thus, we suggest that the extrudate promptly shrinks in the direction of flow (*x*-direction) and expands in the gradient direction

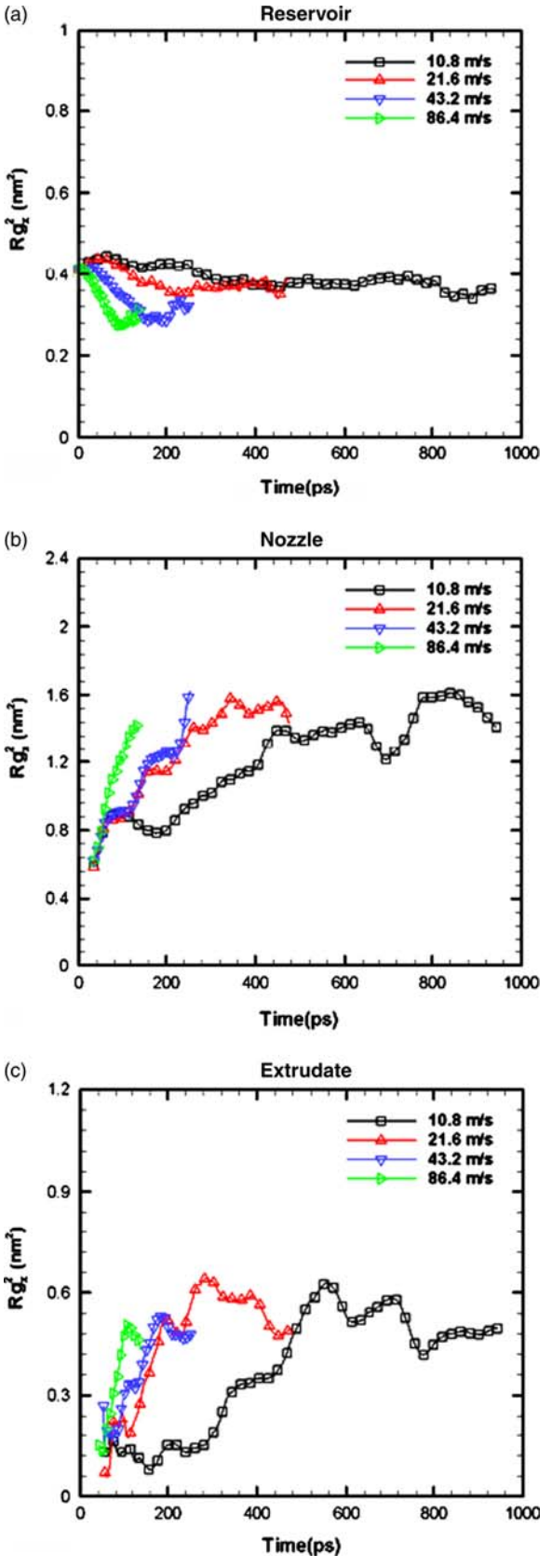

Figure 8. Squared radii of gyration in the x-direction R_{gx}^2 *versus* time t at different extrusion speeds at (a) the reservoir, (b) the nozzle and (c) the extrudate.

(z-direction). As discussed above, the R_g^2 variations can quantitatively demonstrate motions of molecular chains during the flow, and are in agreement with the observation of the snapshots in Figure 3.

As seen in Equation (17), the measure of molecular orientation S [24] is helpful in understanding the direction of molecular chains in flow processes. Notably, S_x is an order of alignment for the end-to-end vector of a molecular chain orientating with the flow (x-axis) direction of the simulation system. When a molecular chain is parallel, random or perpendicular to the flow direction, S_x equals a value of 1.0, 0.0 and -0.5, respectively. As with the previous discussions of R_{gx}^2, the variations in S_x are also analysed in three distinct regions, i.e. the reservoir, the nozzle and the surrounding vacuum.

As shown in Figure 9(a), at the reservoir, S_x decreased with increasing operation time of the piston movement due to the compression of the molecular chains in the x-direction. While the molecular chains at the nozzle were stretched in the x-direction, their S_x increased with the operation time, as shown in Figure 9(b). As a whole, all the values for S_x are close to 0.8. This indicates that the average degree of orientation in the flow direction may be higher for each molecular chain. Thus, a good agreement has been found between our predicted tendency and the related AFM experimental observation [1] of the motion of DNA molecules in microfluidic devices.

After the molecular chains have left the nozzle exit and entered the surrounding vacuum, we inspected, with caution, in Figure 9(b) and (c) that S_x obviously decreased. At the same time, we have also observed in the gradient (z-axis) direction that the S_z value in the surrounding vacuum was close to zero, isotropic. In short, according to the results of the analysis above, we suggest that the degree of the orientation of molecular chains in the flow direction is the highest at the nozzle while it is random in the surrounding vacuum.

3.3 *Flow profiles of a nanonozzle*

When the fluid steadily flows through the nozzle, we would like to understand what the nozzle flow field is, especially the velocity and temperature profiles. Significantly, we noted that variations in the fluid density did not vary acutely with the piston movement and were independent of the extrusion speed; namely, the nozzle density maintained a constant value of about 0.72–0.76 g/cm^3 during the contraction flow process.

First, the nozzle velocity profiles in the z-direction were calculated. The average flow velocity of the fluid can be evaluated by dividing the nozzle domain into a sufficient number of bins. The thickness of each bin is 0.4 nm in the z-direction. The z-direction coordinates of the velocity profiles at the nozzle are scaled between -1 and 1. As shown in Figure 10(a), the velocity profiles are

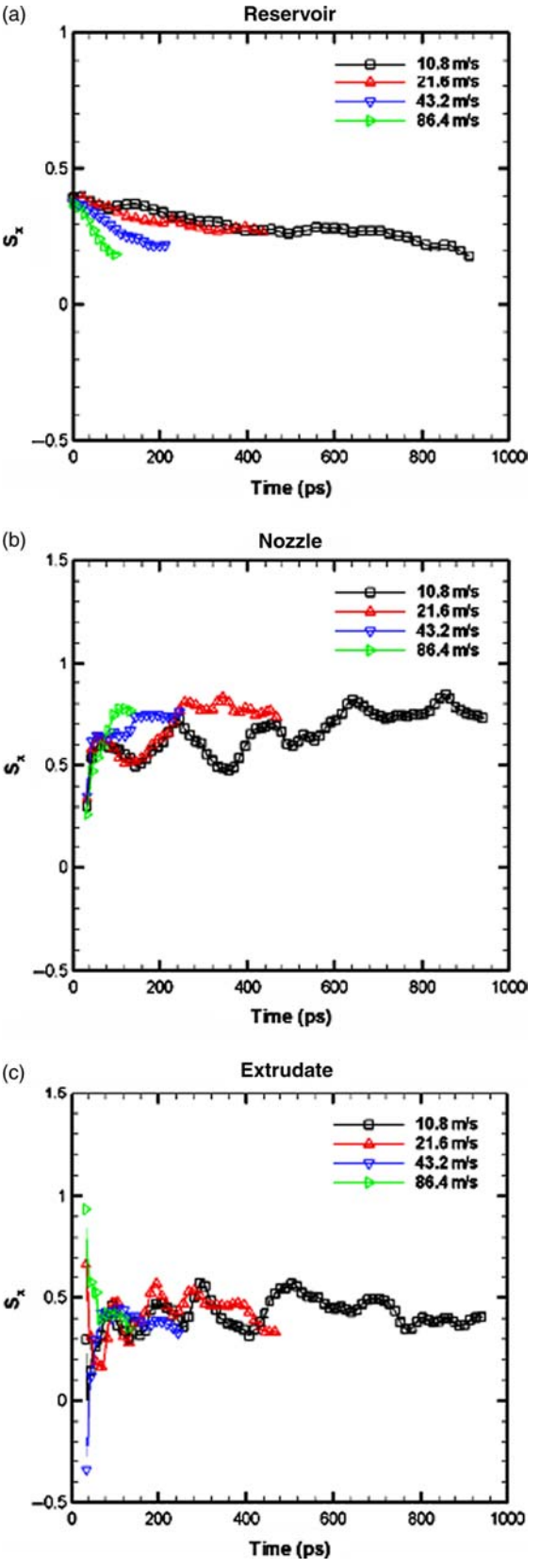

Figure 9. Orientation parameter of the end-to-end vector in the x-direction of S_x *versus* time t at different extrusion speeds at (a) the reservoir, (b) the nozzle and (c) the extrudate.

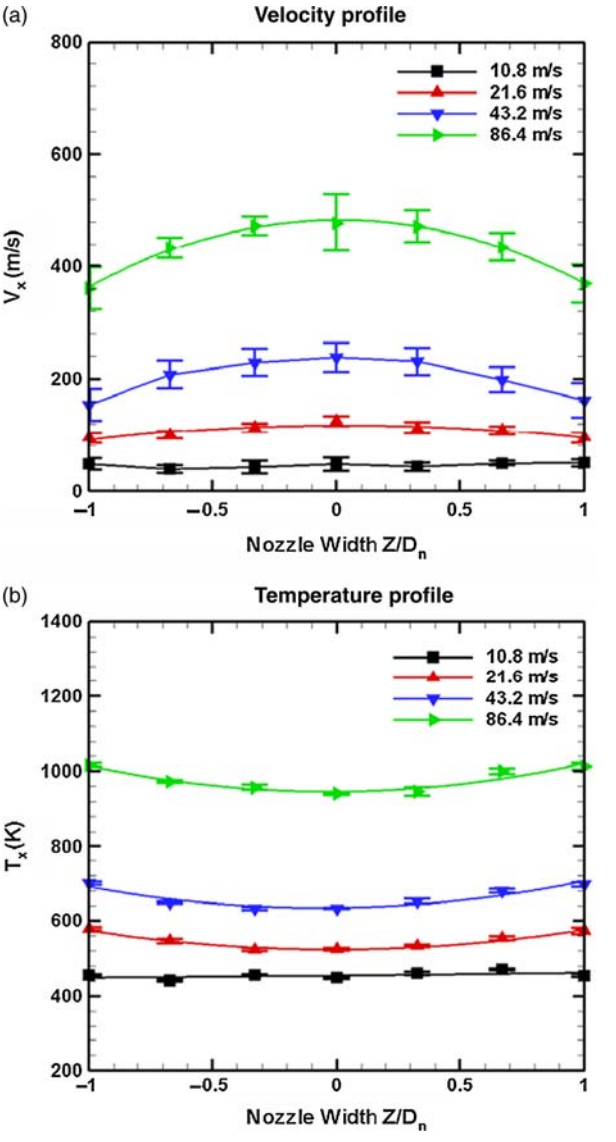

Figure 10. (a) Nozzle velocity profiles and (b) nozzle temperature profiles in the z-direction for a nozzle width D_n of 2.7 nm against the extrusion speeds, obtained when the piston had travelled a distance of 10.11 nm.

at different extrusion speeds and are fit to a second-order polynomial function.

At the lowest speed of 10.8 m/s, the velocity profile presented a similar plug-flow characteristic, namely uniform profile. As expected, a transition of velocity profiles occurred in the range between 21.6 and 43.2 m/s; those profiles were induced to gradually change curves, from plug-like at a lower speed of 10.8 m/s to a somewhat convex parabolic shape. When the speed reached the highest value of 86.4 m/s in the present study, the velocity of the fluid in the centre area of the nozzle was obviously faster than that in the boundary of the nozzle. Such a velocity profile approximated a convex parabolic function, i.e. a characteristic of the Poiseuille flow. Traditionally,

regarding polymer liquids in the capillary rheometer [35], it is well known that the wall slip takes place at a solid surface. Referring to Figure 10(a), a significant wall slip velocity is also clearly observed in the internal boundary of the nozzle while it increased with the extrusion speed.

Experimentally, Shrewsbury et al. [1] showed that by using AFM, when DNA molecules flowed through a planar nozzle in microscale, the nozzle velocity profile was a convex parabolic curve with a central shape that was somewhat flat. It is noteworthy that on an MD simulation research field, Castillo-Tejas et al. [36] and Zhang et al. [37] revealed that as the chain molecules flowed in a nanochannel, their velocity profiles also seemingly presented the plug flow at smaller external forces and the Poiseuille flow at larger external forces, as well as the wall slip occurring near the boundary of the channel. For the nanocontraction expansion flow, Fan et al. [18] found that the nozzle velocity profile is a clear-cut convex parabolic curve when Ar gases flow through a nanonozzle. As a whole, our results are, therefore, in qualitative agreement with their findings.

Eventually, as with the discussions above on the velocity profile graph, the temperature profiles in Figure 10(b) were also fit using a second-order polynomial function. Consequently, the nozzle temperature profile also revealed uniform characteristics across the nozzle width at the lowest extrusion speed of 10.8 m/s. As extrusion speeds pass 10.8 m/s, the temperature profile gradually approaches a concave parabolic function. It is noted that the shapes of the velocity and temperature profiles are inverse, and that the temperature profile slowly approximates a concave parabolic function as the extrusion velocity increases.

4. Conclusions

We have employed MD simulations to report on the nanocontraction flow process for short chains $[CH_2]_{50}$ of PE at different extrusion speeds of 10.8–86.4 m/s. Two significant phenomena have been observed in the present study, namely (1) as many molecular chains were adsorbed on the external surface of the nozzle, this phenomenon should be related to surface wetting in the general physical understanding, (2) as the extrudate diameter was observed to be larger than that of the nozzle diameter, this increase in the diameter of the extrudate is known as similar die swell. As a result, the ratio of the swell and the degree of the wetting decreased with increasing extrusion speed; thus, this result is in qualitative accordance with the experimental actuality of polymer processes.

Under conditions of the fluid at the reservoir being strongly extruded by the piston, the bond length of molecular chains obviously changed with a little variation in the bond angle. Overall, the probability of the equilibrium bond length and the bond angle decreased in conjunction with increasing extrusion speed. As for the dihedral angle, the probability of the *trans* conformation also decreased, whereas the probabilities of both *gauche* and *cis* conformations were almost invariable.

Significantly, observing the motions of molecules during the flow is dramatic; these outcomes are summarised analytically in three points: (1) a moving piston gradually compressed molecular chains in the reservoir; (2) molecular chains were strongly stretched and had the highest molecular orientation of the flow direction when the molecular chains flowed along the flow direction into the nozzle by shear flow; and (3) when the molecular chains exited the nozzle, the molecular chains instantly recovered to the equilibrium state, and their orientation in the flow direction was nearly isotropic. Throughout the preceding quantitative analysis, we used the 'squared radii of gyration' and 'orientation parameters of the end-to-end vector' to inspect the motions of chain molecules, which are in well agreement with the observations of the MD simulation snapshots mentioned above.

Most importantly, at the lowest extrusion speed of 10.8 m/s, both the nozzle velocity and temperature profiles of the fluid obviously presented uniform ones. In contrast to high extrusion speeds over an extrusion speed of 10.8 m/s, the nozzle velocity and temperature profiles became convex and concave parabolic curves, respectively. Moreover, the wall slip behaviour was observed in the boundary of the nozzle area while the degree of the wall slip increased with increasing extrusion speed.

In relation to this, there are some other topics of interest that warrant exploration, such as how variations of system temperature, system geometry and molecular structure affect the contraction flow behaviours. In the future, we expect that the length of molecular chains will be extended to over 200 UAs of the PE fluid, which may generate a very obvious entanglement characteristic to impart the fluid with viscoelastic flow behaviour, thereby increasing the complexity of flow behaviours. Accordingly, the rheological properties of apparent viscosity, normal stress difference and stress distribution can be quantitatively analysed and explained in relation to the flow behaviours of the non-Newtonian fluid. These issues are important fundamental rheological studies. To say the least, observing the motions of coarse-grained DNA molecules in the microchannel will also be a very interesting study, which should be tackled using MD simulation.

Acknowledgements

The authors would like to thank Prof. France Lai of the University of Massachusetts Lowell for helpful discussions during his sabbatical leave at the National Tsing Hua University in 2007. This research was financially supported by the National Science Council of the Republic of China (Grant number: NSC97-2221-E-007-033) and CoreTech System Co. Ltd (Moldex3D).

Note

1. Present address: Science Building 2, 1001 Ta Hsueh Road, Hsinchu 30010, Taiwan.

References

[1] P.J. Shrewsbury, S.J. Muller, and D. Liepmann, *Effect of flow on complex biological macromolecules in microfluidic devices*, Biomed. Microdevices 3 (2001), pp. 225–238.

[2] Y.-J. Juang, S. Wang, X. Hu, and L.J. Lee, *Dynamics of single polymers in a stagnation flow induced by electrokinetics*, Phys. Rev. Lett. 93 (2004), 268105.

[3] E.S.G. Shaqfeh, *The dynamics of single-molecule DNA in flow*, J. Non-Newton Fluid Mech. 130 (2005), pp. 1–28.

[4] C.-T. Han, C.-C. Tsai, T.-A. Yu, and T.-J. Liu, *A finite difference technique for solving the newtonian jet swell problem*, Int. J. Numer. Methods Fluids 15 (1992), pp. 773–789.

[5] J. Sun, N. Phan-Thien, and R.I. Tanner, *Extrudate swell through an orifice die*, Rheol. Acta 35 (1996), pp. 1–12.

[6] W.W. Graessley, S.D. Glasscock, and R.L. Crawley, *Die swell in molten polymers*, J. Rheol. 14 (1970), pp. 519–544.

[7] R.I. Tanner, *Engineering Rheology*, Oxford University Press, New York, 1989.

[8] C.-H. Tsai, H.-T. Chen, Y.-N. Wang, C.-H. Lin, and L.-M. Fu, *Capabilities and limitations of 2-dimensional and 3-dimensional numerical methods in modeling the fluid flow in sudden expansion microchannels*, Microfluid Nanofluid 3 (2007), pp. 13–18.

[9] J.N. Israelachvili, P.M. Mcguiggan, and A.M. Homola, *Dynamic properties of molecularly thin liquid films*, Science 240 (1988), pp. 189–191.

[10] D. Erickson, D. Li, and U.J. Krull, *Modeling of DNA hybridization kinetics for spatially resolved biochips*, Anal. Biochem. 317 (2003), pp. 186–200.

[11] G. Karniadakis, *Microflows and Nanoflows Fundamentals and Simulation*, Springer Science, New York, 2005.

[12] J. Koplik, J.R. Banavar, and J.F. Willemsen, *Molecular dynamics of Poiseuille flow and moving contact lines*, Phys. Rev. Lett. 60 (1988), pp. 1282–1285.

[13] P.A. Thompson and S.M. Troian, *A general boundary condition for liquid flow at solid surface*, Nature 389 (1997), pp. 360–362.

[14] J.D. Moore, S.T. Cui, H.D. Cochran, and P.T. Coummings, *A molecular dynamics study of a short-chain polyethylene melt. I. Steady-state shear*, J. Non-Newton Fluid Mech. 93 (2000), pp. 83–99.

[15] A. Jabbarzadeh, J.D. Atkinson, and R.I. Tanner, *Nanorheology of molecularly thin films of* n*-hexadecane in Couette shear flow by molecular dynamics simulation*, J. Non-Newton Fluid Mech. 77 (1998), pp. 53–78.

[16] G.M. Wang and W.C. Sandberg, *Non-equilibrium all-atom molecular dynamics simulations of free and tethered DNA molecules in nanochannel shear flows*, Nanotechnology 18 (2007), 135702.

[17] H.-C. Tseng, J.-S. Wu, and R.-Y. Chang, *Shear thinning and shear dilatancy of liquid* n*-hexadecane via equilibrium and non-equilibrium molecular dynamics simulations: temperature, pressure, and density effects*, J. Chem. Phys. 129 (2008), 014502.

[18] X.J. Fan, N. Phan-Thien, N.T. Yong, and X. Diao, *Molecular dynamics simulation of a liquid in a complex nano channel flow*, Phys. Fluids 14 (2002), pp. 1146–1153.

[19] M. Moseler and U. Landman, *Formation, stability, and breakup of nanojets*, Science 289 (2000), pp. 1165–1169.

[20] H. Shin, M. Oschwald, M.M. Micci, and W. Yoon, *Influence of thermodynamics state on nanojet break-up*, Nanotechnology 16 (2005), pp. 2838–2845.

[21] S. Murad and I.K. Puri, *Nanoscale jet collision and mixing dynamics*, Nano Lett. 7 (2007), pp. 707–712.

[22] C.-F. Dai and R.-Y. Chang, *Molecular dynamics simulation of thread break-up and formation of droplets in nanoejection system*, Mol. Simul. (in press).

[23] S. Toxvaerd, *Molecular dynamics of liquid butane*, J. Chem. Phys. 89 (1988), pp. 3808–3813.

[24] S. Fujiwara and T. Sato, *Molecular dynamics simulations of structural formation of a single polymer chain: bond-orientational order and conformational defects*, J. Chem. Phys. 107 (1997), pp. 613–622.

[25] S. Chynoweth, R.C. Coy, and Y. Michopoulos, *Simulated non-Newtonian lubricant behaviour under extreme conditions*, Proc. Inst. Mech. Eng., Part J: J. Eng. Tribol. 209 (1995), pp. 243–254.

[26] S. Chynoweth and Y. Michopoulos, *An improved potential model for* n*-hexadecane molecular dynamics simulations under extreme condition*, Mol. Phys. 81 (1994), pp. 133–141.

[27] M.G. Martin and J.I. Siepmann, *Transferable potentials for phase equilibria. 1. United-atom description of* n*-alkanes*, J. Phys. Chem. B 102 (1998), pp. 2569–2577.

[28] M.P. Allen and D.J. Tildesley, *Computer Simulation of Liquid*, Oxford University Press, New York, 1989.

[29] K.J. Tupper and D.W. Brenner, *Compression-induced structural transition in a self-assembled monolayer*, Langmuir 10 (1994), pp. 2335–2338.

[30] R.C. Lincoln, K.M. Koliwad, and P.B. Ghate, *Morse-potential evaluation of second- and third-order elastic constants of some cubic metals*, Phys. Rev. 157 (1967), pp. 463–466.

[31] W.G. Hoover, *Canonical dynamics: equilibrium phase space distributions*, Phys. Rev. A 31 (1985), pp. 1695–1697.

[32] I.C. Carpen, *Microrheology of colloidal dispersions by Brownian dynamics simulations*, J. Rheol. 49 (2005), pp. 1483–1502.

[33] K. Foteinopoulou, N.C. Karayiannis, and V.G. Mavrantzas, *Primitive path identification and entanglement statistics in polymer melts: results from direct topological analysis on atomistic polyethylene models*, Macromolecules 39 (2006), pp. 4207–4216.

[34] P.J. Flory, *Statistical Mechanics of Chain Molecules*, Hanser Publishers, Munich, 1989.

[35] A.V. Ramamurthy, *Wall slip in viscous fluids and influence of materials of construction*, J. Rheol. 30 (1986), pp. 337–357.

[36] J. Castillo-Tejas, J.F.J. Alvarado, G. González-Alatorre, G. Luna-Bárcenas, I.C. Sanchez, R. Macias-Salinas, and O. Manerod, *Nonequilibrium molecular dynamics of the rheological and structural properties of linear and branched molecules. Simple shear and Poiseuille flows; instabilities and slip*, J. Chem. Phys. 123 (2005), 054907.

[37] J. Zhang, J.S. Hansen, B.D. Todd, and P.J. Daivis, *Structural and dynamical properties for confined polymers undergoing planar Poiseuille flow*, J. Chem. Phys. 126 (2007), 144907.